Antenna pointing error and its effect on dynamic range in radio interferometric imaging: Results from simulation

by Subhashis Roy

Internal Technical Report

NCRA-TIFR
Pune-7

Table of contents

Antenna pointing error and its effect on dynamic range in radio interferometric imaging: Results from Simulation

Abstract

Antenna pointing errors could play a significant role in limiting the dynamic ranges achievable with present day radio interferometers. I have carried out a detailed analysis of this limitation using both analytical and simulation methods with particular emphasis on continuum imaging with GMRT data at metre wavelengths. It is found that limitation of dynamic range not only depends on the magnitude of pointing errors, but also on the sidelobe pattern of the synthesised beam. Using typical pointing error of $\sim 1'$ at 90 cm with GMRT, the typical rms error that is reached while observing a typical extragalactic field is ~ 50 μJy, that is about three times higher than the thermal sensitivity of GMRT (32 MHz bandwidth) with full synthesis. In real life, this could worsen by another factor of a few due to pointings done at each of the observing bands including the ones at lower frequencies (e.g., 330 and 150 MHz) leading to poorer pointing accuracies at these frequency bands than is possible at the highest frequency (L) band. This can be improved with a better feed positioning system, along with better tracking accuracy of the servo system.

1 Introduction:

There exists a Fourier transform (FT) relationship that relates the Visibility [$V(u, v)$] obtained after cross-correlating and calibrating the voltages as measured at different antenna locations with the sky intensity distribution $I(l, m)$. This relationship is known as Van-Cittert Zernecki theorem, and serves as the basis for imaging in radio interferometry. It can be expressed as:

$$V(u,v) = \int\int I(l,m) \exp[-2\pi i(\mathrm{ul} + \mathrm{vm})] \mathrm{dl.dm} \tag{1}$$

In the above expression, $I(l, m)$ is the observed sky intensity distribution. Note that the observed sky intensity is a product of the true sky intensity distribution [$I_{\mathrm{true}}(l, m)$] and the primary beam pattern of the antennas [$A(l, m)$]. For Eq. 1 to remain consistent for visibilities acquired through different pair of antennas, $I(l, m)$ must be the same for all the antennas. This requires two conditions, (i) The primary beam pattern (A) must be same for all antennas, and (ii) all the antennas must be pointing to the same direction of the sky so that their direction cosines (l, m) is the same.

For typical antennas used in working interferometers at cm to metre wavelengths (e.g., WSRT, VLA or GMRT), all the antennas in a particular array are made following the same design, and hence the primary beam pattern is expected to be the same for all the antennas. However, due to mechanical limitations, if different antennas point at slightly different directions, $A(l,m)$ need to be written as $A(l_i,m_i)$, where i is the antenna number, and in general will differ among antennas. This causes pointing error and different antennas "see" different flux-densities of sources as a function of angular distance from the *actual* pointing centre of each antennas. A pointing error of 5% of the antenna primary beam width causes flux density of sources seen near FWHM to change by $\sim$15%. This pointing accuracy has typically been considered as acceptable at the highest frequency of operation in existing interferometers (Synthesis imaging in Radio Astronomy, ASP Conf. Ser., 180, chap. 3, p51) built more than a decade back. Presence of $\sim$15% error in source flux densities at FWHM in the highest observing band that progressively gets small at longer wavelengths may not be a serious problem, but failure of Equation (1) causes artefacts during deconvolution using that equation, and reduces the dynamic range of maps from radio interferometric data. At higher radio frequencies (>1.4 GHz), the primary beam of typical parabolic antenna based interferometers are quite small ($\lesssim 30'$, for GMRT, VLA and WSRT), and often the target source is at the centre of the beam. Consequently, the effect of pointing errors is less important at higher frequencies. However, with emphasis on high dynamic range low frequency observations with the existing facilities like the GMRT and other upcoming facilities like ASKAP, it has become important to quantify the effect of pointing error on image dynamic range, and this report is expected to address that. Analysing its effect in the map plane is complex. I would analyse it from simple analytical and simulation models.

2 Analytical models of Pointing errors:

2.1 Single source with a single dish

To make a best fit to a parabolic antenna primary beam pattern within the main lobe, often a polynomial is used. However, as shown in Fig. 1, it is pretty close to a Gaussian for GMRT antennas. Therefore, to keep the analysis simple, we consider a Gaussian Primary beam pattern.

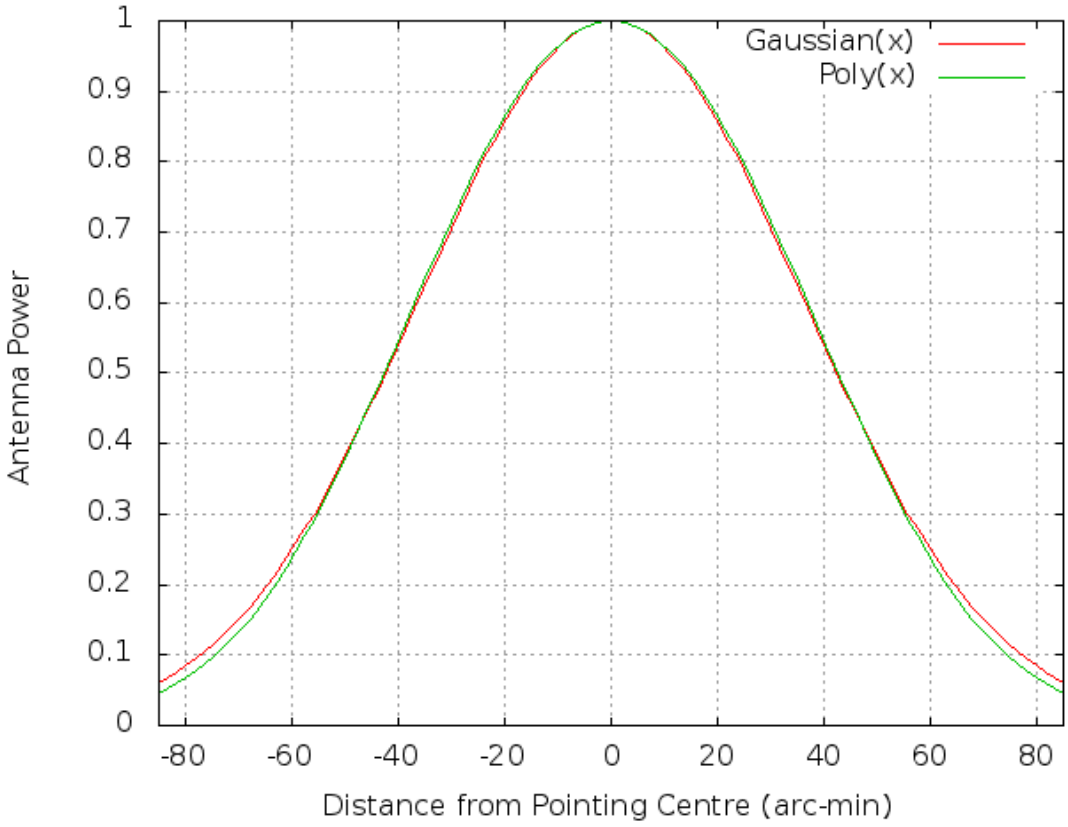

Figure 1. Plot of GMRT antenna response at 330 MHz approximated with the standard Polynomial fit used for primary beam correction (Green) versus a Gaussian (Red).

Then, we can express flux density (S) of a source seen at an angle θ from the axis as

$$S(\theta) = S_0.\exp\left(-\frac{\theta^2}{2.\sigma^2}\right), \tag{2}$$

where, S_0 is the true flux density of the source, and σ is related to the FWHM of the Gaussian function by $\sigma = 0.42 \times \text{FWHM}$. In this report, we denote σ as half beam width.

Change in normalised flux density of a source due to small change in θ ($\Delta\theta$) is obtained by differentiating the above:

$$\frac{1}{S_0}\Delta S(\theta) = -\left(\frac{\theta}{\sigma^2}\right)\exp\left(-\frac{\theta^2}{2.\sigma^2}\right).\Delta\theta$$

From above, we find that error in flux density (ΔS) for a fixed pointing error $\Delta\theta$ depends on the relative angular offset (θ) of the source with respect to the beam-width ($\sim 2\sigma$). Peak occurs at $\theta = \sigma$. As beam width is inversely proportional to

frequency, we substitute $\sigma \propto \frac{\sigma_1}{\nu}$. As ΔS depends on the relative angular offset of the source with respect to the beam width, we define $\frac{\theta}{\sigma} = \Theta$. Where, σ_1 corresponds to beam-width at 1 GHz, and Θ denotes angular offset normalised by the beam-width.

$$\Delta S = S_0.\nu.\frac{\Theta}{\sigma_1}.\exp\left(-\frac{\Theta^2}{2}\right).\Delta\theta \tag{3}$$

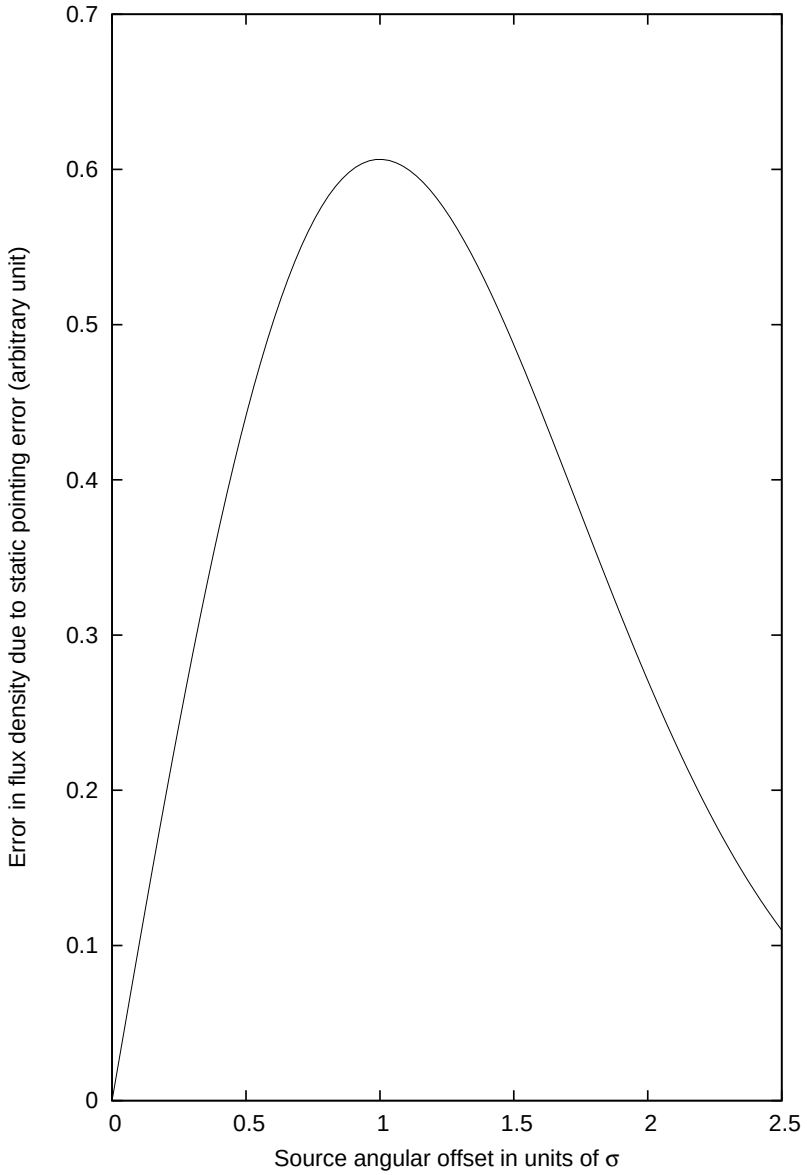

Figure 2. Flux density error due to mis-pointing ($\nu = 1$).

From (2), we find that flux-error (ΔS) for the same angular offset is proportional to frequency. A plot of Eq. (2) assuming ν is unity is shown in Figure 2. From Fig. 2, we find that the pointing error remains above half its maximum value for $0.3 < \Theta < 1.9$, indicating significant contribution to pointing error from most of the sources within twice the primary beam area.

2.2 Contribution of pointing error in limiting dynamic ranges of interferometric maps:

From inverse of Eq. (1), one can write source intensity as in a Dirty map (I_D) in terms of a Fourier series.

$$I_D = \frac{1}{M}\sum_{k=1}^{M} V(u_k, v_k).e^{2\pi i(u_k l + v_k m)} \tag{4}$$

where, u_k, v_k are the points in the u, v plane where visibility measurements exists, and M is the total number of visibilities ($M \propto N(N-1)/2$, where N is the no. of antennas in the array). By defining the sampling function, $S = \sum_{k=1}^{M} \delta(u - u_k, v - v_k)$, it can be shown that $I = B * \mathrm{FT}(V)$, where B is the FT of S.

Order of magnitude estimation of dynamic range

I first consider pointing error for one of the antennas (n) that results in flux density error of $\sim\Delta S$ for a single point source in the primary beam of the antenna. The flux density as measured in total power for antenna 'n' is $S(1+\Delta G)$. Where, $\Delta G = \frac{\Delta S}{S}$, and results in an error of $\frac{\Delta G}{2}$ in the voltage gain of that antenna. Since the error under consideration occurs in amplitude, it would appear as an amplitude gain error, that is symmetric around a source. One can do a phase shifting of the source visibilities so as to image it at the phase centre. In this case, assuming no noise or other artefacts in the data, the resultant Dirty image can be expressed as:

$$I_D(l,m) = \frac{1}{M}\left(\sum_{k=1}^{M} V_I(u_k, v_k)\, .e^{2\pi i(u_k l + v_k m)} + \sum_{i=1, n\neq i}^{N-1} \frac{\Delta S}{2}(u_{\mathrm{in}}, v_{\mathrm{in}}).e^{2\pi i(u_{\mathrm{in}} l + v_{\mathrm{in}} m)} \right) \tag{5}$$

In the above, we have considered only one time-stamp, so that $M = N(N-1)/2$. One can find the first part is the standard expression of a Dirty image. By subtracting the synthesised beam pattern during Clean deconvolution, the diffraction pattern for the source from the map will be removed. However, the second term indicates the Dirty image formed by using data having erroneous flux density $\left(\frac{\Delta S}{2}\right)$ as contained in all the visibilities with that antenna.

Since the no. of visibilities that is contributed by one antenna in an array with N elements at any instant is $(N-1)$, the error in the dirty map at the position of the source will be $\sim\frac{\Delta S.(N-1)}{2} \div \frac{N.(N-1)}{2} = \frac{\Delta S}{N}$. Assuming $N \gg 1$ (as in any modern radio interferometers), error in flux density at the position of the source is much less than what is seen by the particular antenna with pointing error. Therefore, we can consider the flux density of the Clean component at the position of the source that is picked up by CLEAN during deconvolution is the right flux density for the source. Clean then subtracts the diffraction pattern of the source components with the right flux density. This would take away the diffraction pattern for all baselines except the ones formed by including the antenna having pointing error. If we define the beam of the sampling function that is formed with all the baselines with that antenna as B_n, then the error pattern left on the map as in second part of Eq. (5) is

$$\sim\frac{\Delta S.B_n(p,q)}{N}, \tag{6}$$

where N in the denominator appear due to normalisation as denoted by 'M' in Eq. (4). It has to be noted that the beam pattern except at its origin is oscillatory going through positive and negative values. During imaging, if data weights near the boundaries of UV plane where data exists are suitably tapered to avoid ringing due to sudden cutoff in data, and if the antennas are placed such that the UV coverage generated by different baselines are close to being random in UV plane, the side lobes from beams as formed by different baselines add randomly in the map plane. Therefore, sidelobe amplitudes in dirty beam is almost inversely proportional to the square root of the number of baselines involved in forming the beam. Therefore, we can write

$$B_n(p,q) \sim \sqrt{\frac{N}{2}}.B(p,q) \tag{7}$$

, where p, q (p, q are outside the main lobe of the synthesised beam) are the position of any point in the map in pixels along East and North with the centre of the coordinate being coincident with the beam centre. Therefore, the error that is left in the map plane in general can be obtained by replacing B_n in Eq. (6) by B from Eq. 7 and is $\sim\sqrt{\frac{1}{2N}}.\Delta S.B(p-p', q-q')$. Where, p' and q' are the pixel based coordinate of the source. Pointing errors being antenna based, when all the antennas suffer from pointing errors, errors from them will add randomly in the map plane. If ΔS is the rms error in flux density by different antennas due to pointing error of a source, then at a position $p-p', q-q'$ pixels away from the source, the map error as computed for a single antenna need to be multiplied by $\sqrt{N}$. Then we get,

$$\text{Map rms} \sim \frac{1}{\sqrt{2}}\Delta S.B(p-p', q-q') \tag{8}$$

2.3 Multiple sources:

Since there are many sources in sky, it is important to estimate their overall contribution. Strong sources contributes mostly to the pointing error (e.g., Eq. 3). Typically GMRT can detect mJy sources at metre wavelengths. However, the sources with flux densities of hundreds of mJy or more contribute largely to the pointing error. These sources being $>>5\sigma$, they are seen almost up to twice the primary beam of the antennas. Therefore, their detection is not significantly dependent on the primary beam attenuation at least up to the FWHM, that is close to the effective beam area. It is known that source number density (k) above a certain range of flux densities (say $>10\sigma$) is proportional to the area of the sky being observed. Also, from Fig. 2, pointing error from sources in most parts of the primary beam is similar (within a factor of two). Therefore, map rms would be proportional to the square root of the no. of sources (K) present in the primary beam. One can write, rms $\propto\sqrt{K}.\Delta S$, and as the primary beam area is inversely proportional to the square of the observing frequency, $\sqrt{K} \propto\nu^{-1}$. After substituting the expression of ΔS from Eq. (3), we get

$$\text{rms } \propto\nu^{-1}.\nu.S_0\frac{\Theta}{\sigma_1}.\exp(-\Theta^2).\Delta\theta.$$

In the above case, all the terms except S_0 are frequency independent. As $S_0 \propto\nu^{\alpha}$, where α is the spectral index and is ~-0.8 for typical extragalactic radio sources, we finally get map *rms* $\propto\nu^{-0.8}$. This implies that images made at lower frequencies will be more affected by pointing errors of the antennas. For GMRT, the most sensitive lowest frequency band is at 330 MHz. Therefore, in this report we will consider the limitation from pointing errors for this band only. For other bands, the map rms can be estimated by scaling with $\nu^{-0.8}$.

3 Simulation of Pointing error:

In Sect. 2.2 we found the map rms due to pointing error depends on the synthesised beam, and that in turn depends on (i) the array, (ii) the location of the source in the sky and (iii) the hour angle range of the source being tracked. Moreover, the pointing error could be time variable and the typical sky imaged away from the Galactic plane shows a large number of sources within the primary beam with varying source strength. These cases are of significant practical importance, but is difficult to analyse using analytical methods. It is, however, traceable by using simulated data for a particular array. I used locally developed software 'gsim' (developed by Kshitija Deshpande and A. Pramesh Rao) for simulating Pointing and Calibration errors. I first simulate a few of the simple cases as described above, and examine the results. A more realistic model involving distribution of extragalactic source counts in the primary beam and resultant dynamic range limitation given a typical rms pointing error of the GMRT antennas is described in Sect. 3.4. In all these simulations unless mentioned specifically, the rms random noise that is added to the model data is about an order of magnitude lower than the expected thermal noise in real data from GMRT.

3.1 Systematic error in visibility amplitude due to a fixed azimuth or elevation error in an antenna

Using 'gsim' we show in Fig. 3 a plot of the generated UV data amplitude when one of GMRT antenna, C00 is having a 6′ error in its elevation angle at 330 MHz and a calibrator source is assumed near the half power position of the antennas with Declination (J2000) of 19°36′00″. Fig. 4 shows the effect of an azimuth error of 6′ for the same antenna when the same source was along the antenna axis.

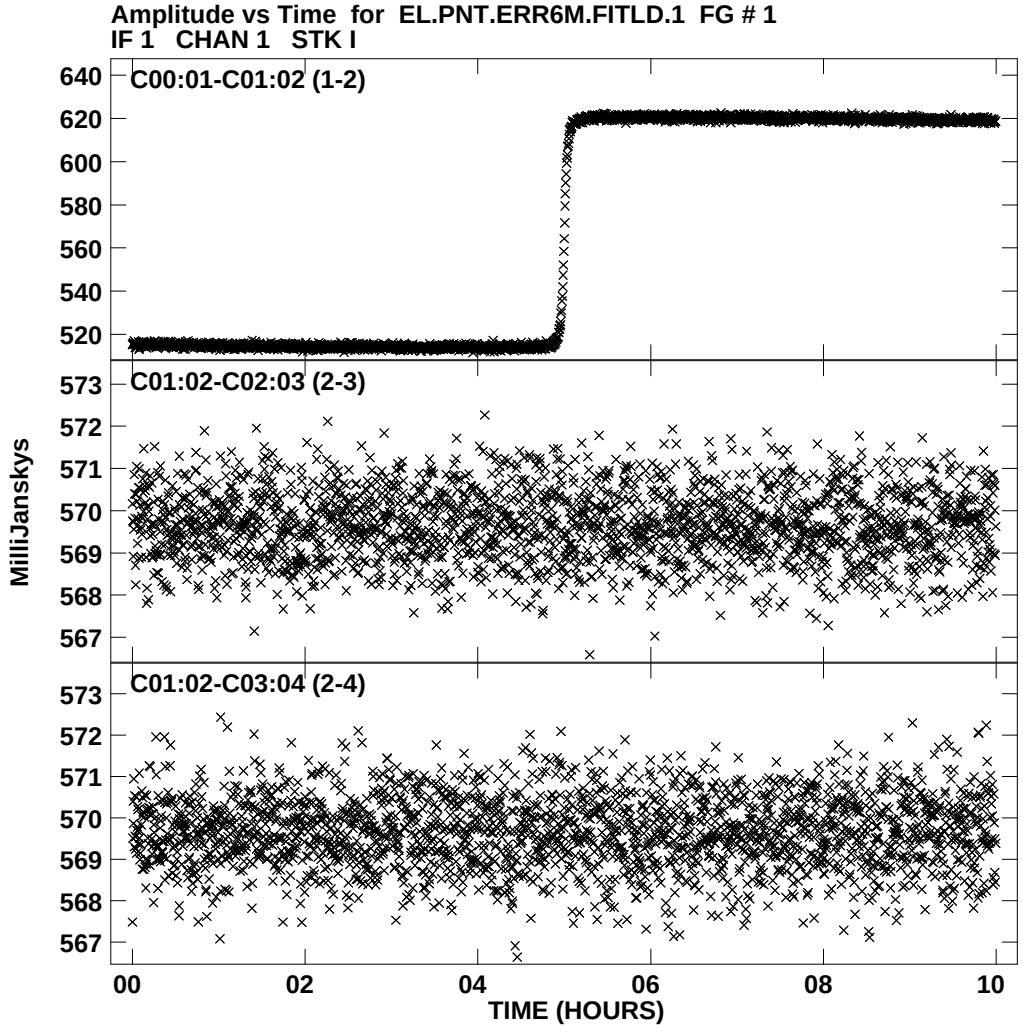

Figure 3. Amplitude variation of source flux density in different baselines due to 6′ elevation error of antenna C00 at 330 MHz. Source is simulated to be near half power point.

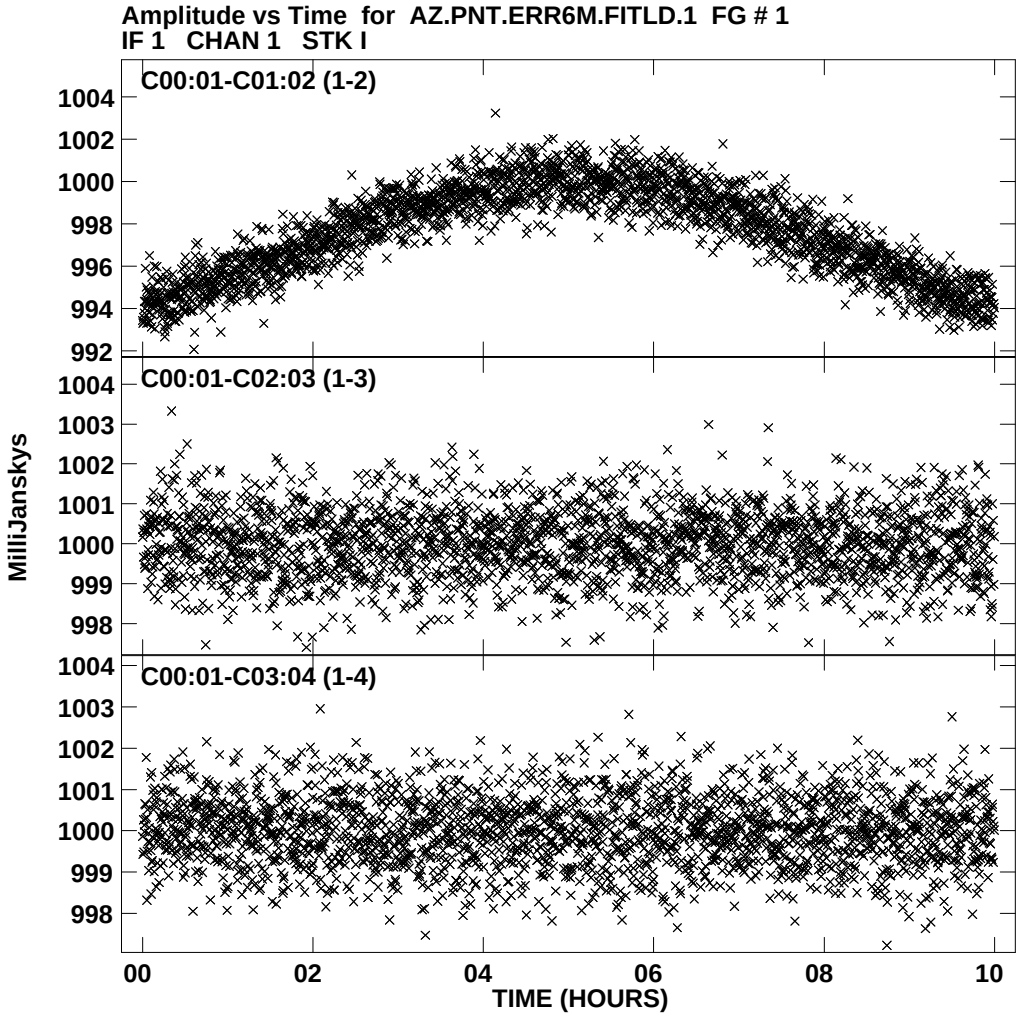

Figure 4. Amplitude variation of source flux density in different baselines due to 6′ azimuth pointing error of one of the antennas (C00) at 330 MHz. Source is simulated at the pointing centre.

3.2 Systematic error on map from a fixed elevation error:

I simulated a case with 1′ error in elevation pointing for all the GMRT antennas. The source is simulated to be of 1 Jy and placed at the half power point of the antennas at 330 MHz. In case of Alt-Az mount, any source not at the pointing centre rotates within the primary beam with paralactic angle. In presence of pointing error, its angular distance from antenna axis changes as a function of paralactic angle causing the source flux density to vary with it. The resultant map is shown in Fig. 5. The UV-coverage was simulated for a source with declination of 19.6° that passes nearly overhead at the location of the GMRT. The rms noise measured ∼10′ away from the source is $\sim 50\,\mu$Jy.beam^{-1}. At this angular distance from the beam centre, the sidelobe rms of the synthesised beam is measured to be about 0.003. As the source is at half power point, $\Delta S \sim 0.025$ Jy. Therefore, the expected rms noise in the map ∼10′ away from the source is expected to be 53μJy.beam^{-1} (Eq. 8), and is close to what is actually found from the simulation.

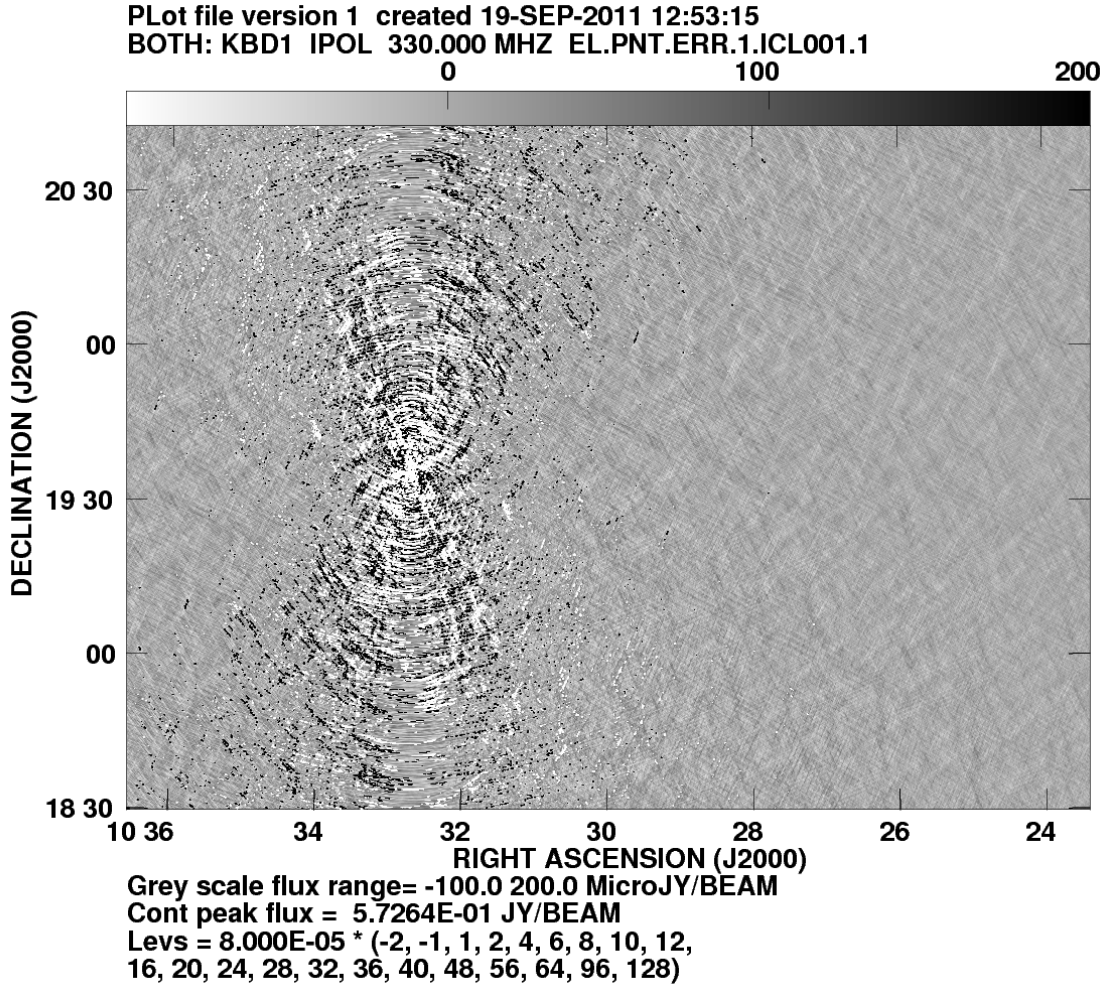

Figure 5. Full synthesis Clean map with a 1 Jy source near Half power at 330 MHz with all the antennas having a fixed $1'$ elevation error. Rms noise $\sim 10'$ away is $\sim 50\,\mu$Jy.beam^{-1}.

Very similar result was obtained with antennas having offsets $\pm 1'$ distributed randomly.

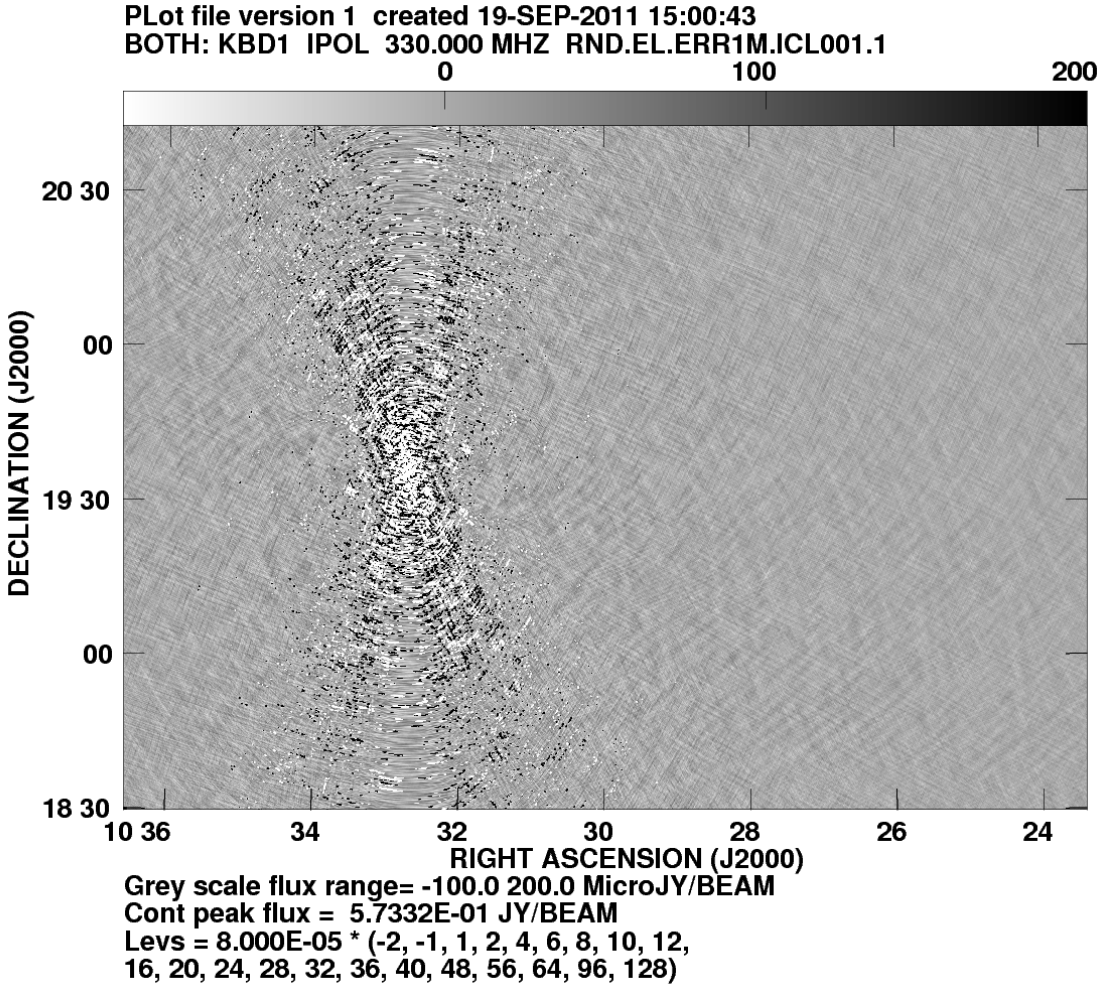

Figure 6. Same as in Fig. 5 except antennas having elevation error ($\sim 1'$) changing in 1 hour timescale. Rms noise $\sim 10'$ away from the source is $\sim 33\,\mu$Jy.beam^{-1}.

With pointing errors changing in shorter timescales, we find that systematic patterns in maps reduce. However, rms noise remains quite similar to the above.

3.3 Dependence of dynamic range with sidelobes of synthesised beam

In order to check the dependence of image rms with the synthesised beam, we also simulated a snapshot observation with the above data within ±0.5 hour of its zenith crossing time of the source. Fig. 6 shows the map made from the data. The rms noise on the map $\sim 10'$ away from the source is $\sim 300\,\mu$Jy.beam^{-1}. Due to poorer UV coverage in a single snapshot, synthesised beam was found to have a factor of 6 higher sidelobe amplitude that resulted in a factor of 6 higher rms due to Pointing error.

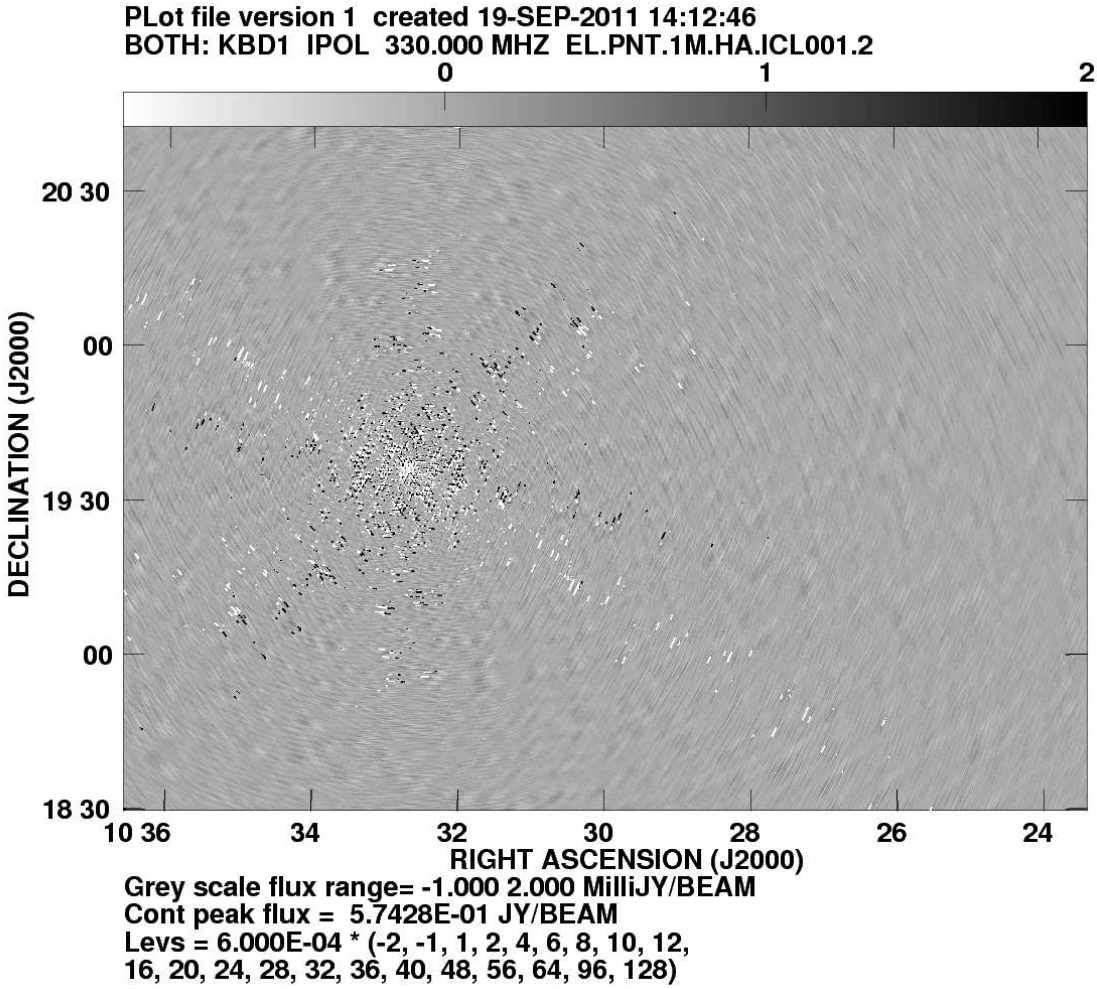

Figure 7. Clean map made from the same data within ±0.5 hour of change of Elevation offset. Rms noise $\sim 110\,\mu$Jy.

3.4 Dynamic range limitation while observing typical extragalactic fields due to pointing error

To determine the affects of pointing errors in maps made with GMRT data, one need to generate simulated data with pointing errors from different sources in typical fields with different UV coverages resulting from different declinations of observing fields. The nature and magnitude of pointing error is discussed below followed by simulation of typical extragalactic sky using known logN-logS distribution of sources.

3.4.1 Static and dynamic pointing error

The typical pointing error as observed with GMRT antennas has two components, with the static component relatively stable over a few days, and the dynamic part that varies as a function of azimuth and elevation angles of the antennas. Therefore, practical simulation need to consider the dynamic component along with the static component discussed above. The designed tracking accuracy of the GMRT is taken to be $1'$. This is however a typical lower limit, as any offset that is ill determined adds up as static pointing errors. Considering the above value, pointing offset measurement limitations using calibrators could leave a residual static pointing error of $\pm 1'$ in both elevation and azimuth at the highest frequency of operation. Due to limitation of tracking systems during observations, another $1'$ of dynamic error that could also vary due to unmodelled changes in antenna structure (e.g., gravitational bending) or geometrical errors in antenna axis that causes change in pointing offsets with azimuth and elevation angle is likely to be introduced. Since significant change in azimuth and elevation angles occur in a timescale of $\sim$1 hour, we have taken the

timescale of the random pointing error variation as two hours. In the simulation, we have used $1'$ error in both elevation and azimuth as static errors, and another $1'$ error as time variable error with timescale of two hours of variation. The simulation software do consider this timescale according to a Gaussian probability distribution (see Fig. 8), where σ equals the timescale as mentioned.

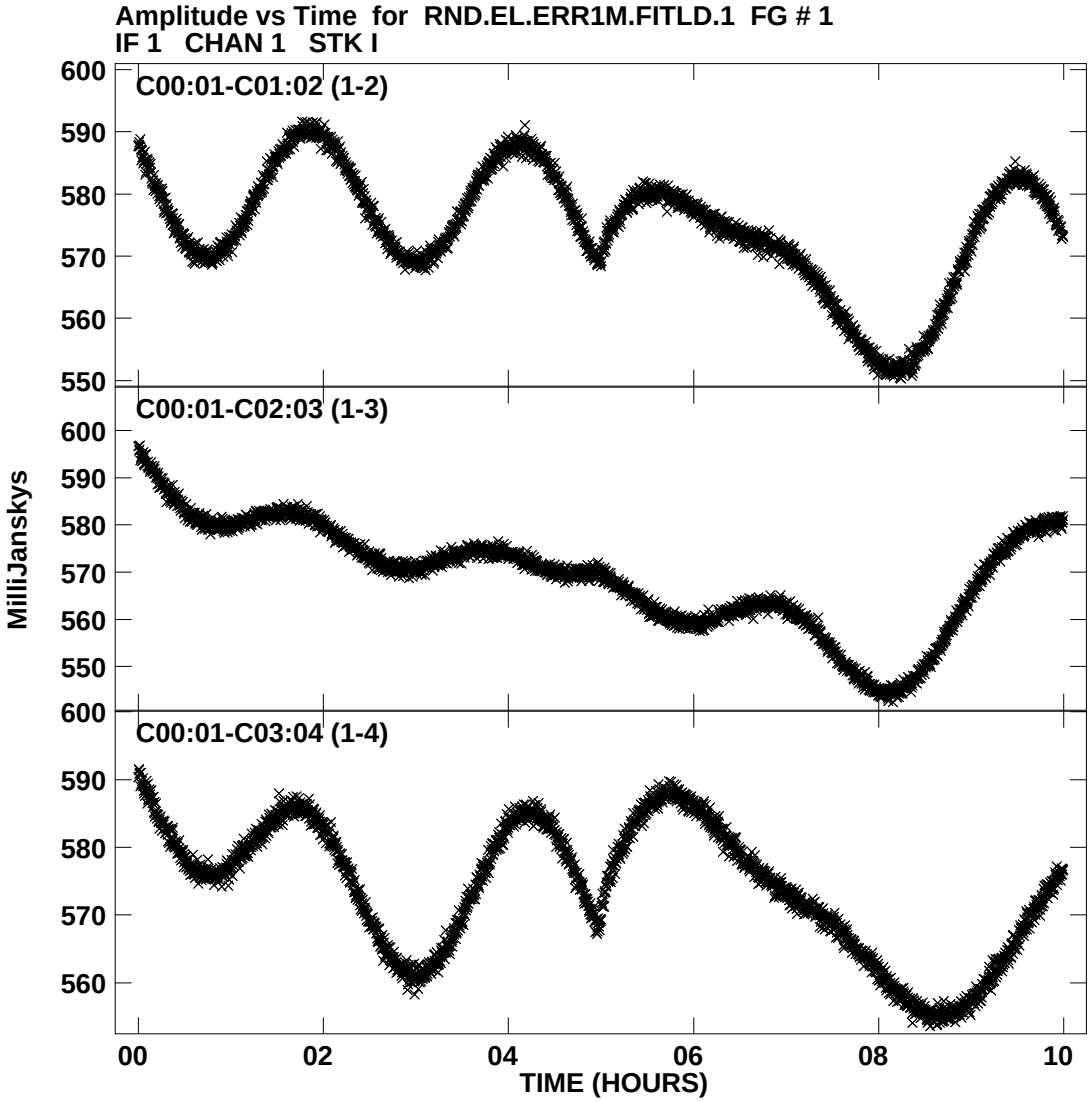

Figure 8. Plot of simulated data with a 1 Jy source near Half power and antenna elevation error changes by $\sim\pm1'$ in timescales $\sim$1 hour.

3.4.2 Simulating pointing error with sources following logN–logS distribution in field of view

To check for the typical rms error due to antenna mis-pointings at metre wavelength with GMRT, typical extragalactic sky need to be simulated. I have used a soft-

ware 'newsimgmrt' that was locally developed by Vasant Kulkarni. Using a random number generator, it generated a set of random distribution of sources following known logN − logS distribution at 408 MHz and scaled by a spectral index of -0.8 (Flux density $\propto \nu^{\alpha}$, where ν is frequency and α is the source spectral index) of extragalactic sources for the given frequency in twice the angular diameter of the GMRT primary beam at that frequency. To reduce the bias in rms noise due to positions of stronger sources in the field, we generated a set of nine random distribution of sources at 330 MHz, and used first 3 sets of such sources at for a Declination of $+60°$, the next 3 set of fields at Declination of $+15°$ and the next set of 3 fields at Declination of $-30°$ with 'gsim' to generate model UV data. The RA used during simulation was 10h30m00s (UV coverage for any field is independent of the RA used). I used 10 mJy as the lower cutoff of source flux density in this simulation. Typically ∼350 sources were generated with a flux density $\geqslant$10 mJy at 330 MHz within a radius of 1.5° from the beam centre.

While using 'gsim' with the modelled sources discussed above, random noise of 15 mJy was added to each data points (assumed integration time of 16 seconds and an effective bandwidth of 27 MHz) that would correspond to $\sim 15\,\mu$Jy.beam^{-1} expected in the map plane from observations with the above effective bandwidth of 27 MHz and and an observing time of about 10 hours. I did not introduce any W term in the UV data, so that simple 2-D imaging technique can be used. Within the simulated fields, there were typically $\sim 3-4$ sources of strength ∼1 Jy, that would cause a significant part of the systematic errors on an interferometric map due to pointing errors.

3.4.3 Results

Using the simulated UV data for all the fields at 3 different Declinations we imaged the fields using standard Clean. Table 1 shows the details of the fields imaged and the rms obtained in each of the maps.

Table 1. Details of the simulated fields imaged

Field No.	No. of sources	Dec. (deg)	Peak flux (Jy)	Peak negative (mJy)	Rms noise (μJy.beam^{-1})
1	357	60	0.73	−1.8	44
2	328	60	0.63	−1.5	50
3	361	60	0.64	−1.2	49
4	305	15	0.45	−1.2	32
5	350	15	0.60	−2.1	48
6	354	15	0.85	−2.3	52
7	359	−30	0.76	−1.1	40
8	330	−30	3.77	−2.1	67
9	368	−30	0.57	−1.7	50

Contour map of one these fields (Field 5) is shown in Fig. 9.

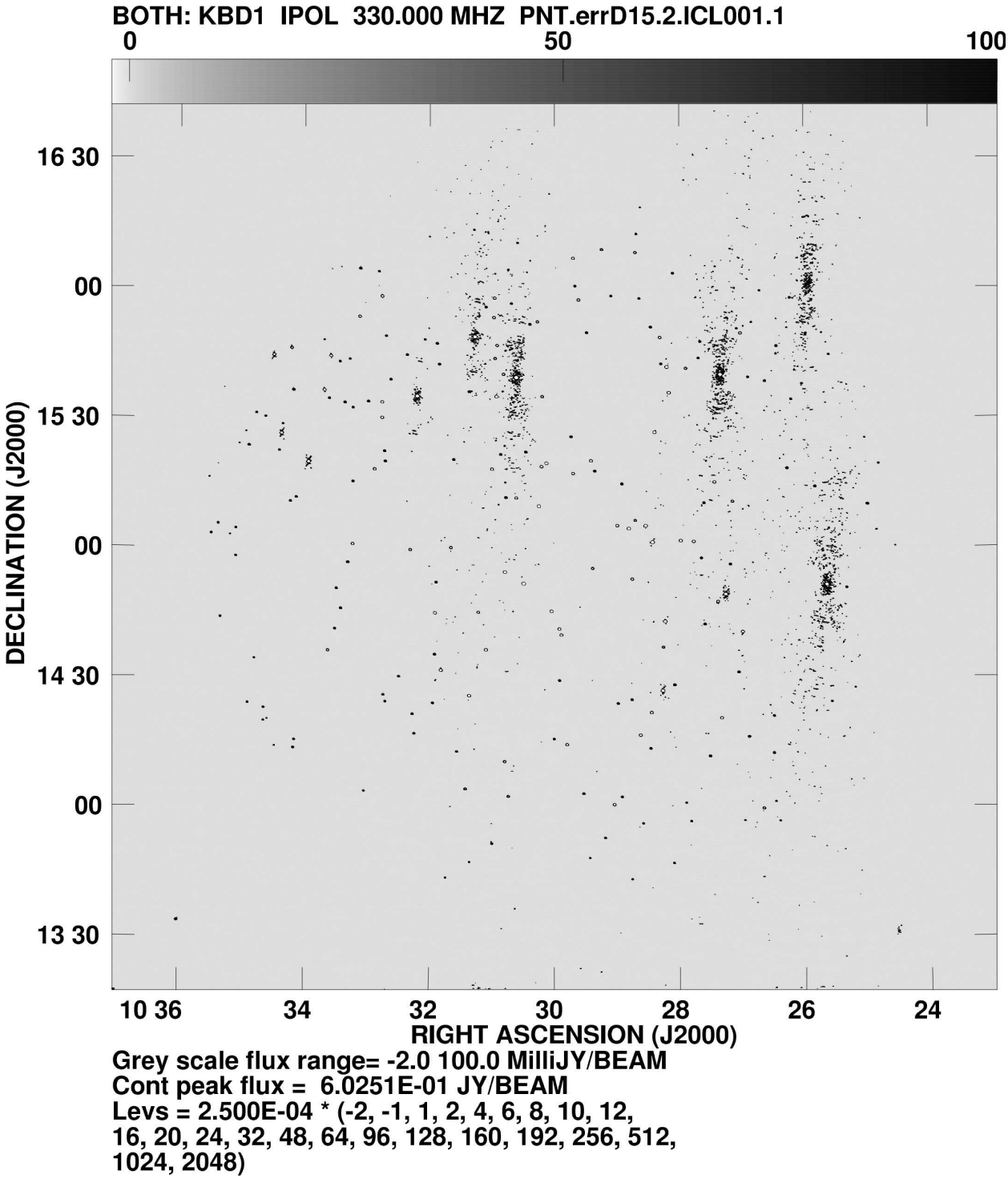

Figure 9. Full synthesis map from the simulated Sky data for Field 5 with random and systematic error of $\sim 1'$ in elevation and azimuth. A random noise corresponding to a theoretical noise of $\sim$15 μJy was added during simulation. The above map due to systematics has an rms noise $\sim$48 μJy.

It can be seen from Table-1 that the mean rms noise from all these 9 fields is 48 ± 3 μJy.beam^{-1}. This indicates that the rms of the systematics due to pointing error produced on a map while observing a typical extragalactic field is not much affected by the distribution of stronger sources within the primary beam.

4 Implications and possible solutions:

Thermal noise with an effective bandwidth of 80% of the 32 MHz passband that GMRT supports at 330 MHz is 15μJy over an observing time of 10 hours. Clearly the rms noise due to systematics produced from pointing error is more than 3 times higher and is likely to be one of the most important parameter limiting the present day sensitivity of the telescope at meter wavelengths. In fact, a major source of pointing error at lower GMRT frequencies is caused by unknown fixed offsets for each feeds of the antennas after feed rotation. To circumvent this, pointing offsets of the antennas are determined from calibrator observations even at lower frequency bands. However, the primary beam of the antennas get broader at lower frequencies and at 330 MHz, the uncertainty in determining static offsets is $\sim$4 times than that at 1280 MHz. Since the uncertainty in pointing offset determinations at 1280 MHz is $1'$, this uncertainty would be $\sim 4'$ at 330 MHz. Consequently, the rms noise in maps made at 330 MHz could get limited to a few times higher than 50 μJy.beam^{-1}.

Major efforts need to be taken to ensure a reliable feed rotation system that can rotate the feeds to desired accuracy and pointing offsets determined at the highest observing frequency (L band) can be used at the lower observing frequencies after a feed rotation. Also, reducing errors in tracking the antennas from $1'$ to $20''$ will remove the major part of the dynamic pointing error ($\sim 1'$). There exists imaging algorithm that does direction dependent self-calibration of each antennas (Bhatnagar et al., 2008, A&A, 487, 419) that could reduce this problem. The technique of Peeling could also be tried to address this problem.

Acknowledgement

The software 'gsim' that was used in this simulation was written by Kshitija Deshpande and A. Pramesh Rao. I thank them for their contribution. Vasant Kulkarni wrote the programme 'newsimgmrt' that was used to generate the sources in the fields, and I also thank him for his contribution.